Declaration

I hereby declare that the work presented in this Thesis titled *Self-assembly of Surfactants and Bio-inspired Soft Materials for Desired Macroaggregates using Multiscale Simulations* submitted to the Indian Institute of Technology Jodhpur in partial fulfilment of the requirements for the award of the degree of Doctor of Philosophy, is a bonafide record of the research work carried out under the supervision of Dr. Ananya Debnath. The contents of this thesis in full or in parts, have not been submitted to, and will not be submitted by me to, any other Institute or University in India or abroad for the award of any degree or diploma.

Arpita Srivastava
P15CY006

Certificate

This is to certify that the thesis titled *Self-assembly of Surfactants and Bio-inspired Soft Materials for Desired Macroaggregates using Multiscale Simulations*, submitted by *Arpita Srivastava (P15CY006)* to the Indian Institute of Technology Jodhpur for the award of the degree of *Doctor of Philosophy*, is a bonafide record of the research work done by him under my supervision. To the best of my knowledge, the contents of this report, in full or in parts, have not been submitted to any other Institute or University for the award of any degree or diploma.

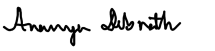

Ananya Debnath
Ph.D. Thesis Supervisor

Acknowledgments

Creating a Ph.D. thesis is not an individual experience, rather it is an outcome of the extreme hardwork of several persons. I pay my most sincere and heartfelt gratitude to everyone who have made this thesis possible. I would first like to extend my most sincere thanks and appreciations to my thesis supervisor Dr. Ananya Debnath for providing me chance of a lifetime to become a part of her research group and introducing me to this exciting scientific field. My entire Ph.D. journey would have been unthinkable without her advice, dedicated support, motivation and enthusiasm. Her integral focus on research and the aim for producing high-impact work has deeply influenced me. I am profoundly grateful to her for always being a strong support at both professional and personal levels.

I would like to thank Dr. Debapratim Das, Professor, IIT Guwahati, and his entire research group for all the experimental supports and their excellent co-operation. I am grateful to Dr. Sriram Goverapet, TCS Research and Dr. Bidisa Das, IACS Kolkata for helping me in the quantum chemical calculations. Their invaluable contributions have enabled me to bring out the best from my research projects. My special thanks also go to faculty members of the Soft Matter Journal Club Dr. Ananya Debnath, Dr. Santosh Mogurampelly and Dr. Prabhat Jaiswal for concieving the idea of a common platform for discussions in the Soft Matter domain. I would also like to thank my committee members Dr. Manikandan Paranjyothy, Dr. Samanwita Pal and Dr. Satyajit Sahu at IIT Jodhpur.

I wish to acknowledge the wonderful support which I have received from my labmates and also my co-authors Mr. Raju Lunkad, Dr. Abhinav Srivastava and Mr. Avinash Garg. Working with them as a team has been a great pleasure to me. I am also thankful to my all other labmates Ms. Aishwarya, Ms. Sheeba, Ms. Neha, Ms. Purva, Mr. Parveen, Mr. Piyush and Ms. Renu for being the best support during the tough times. I am heartfully thankful to all my PhD colleagues Mrs. Manju, Dr. Deepak, Ms. Erum, Ms. Bhawna, Ms. Sumitra, Ms. Anchal, Ms. Divya, and Mr. Amitap for sharing my most cherishable moments with them. I would also like to thank Mr. Anil Kumar, Mr. Krishna Kant, Mr. Rinkesh Mangal, Mr. Rimpesh Katiyar, Mr. Dheerendra Yadav, Mr. Shubham Pandey, Mr. Ganpat Chaudhary, Ms. Swati Kushwaha and Mr. Sandeep Gehlot for their assistance regarding the technical and non-academic tasks.

I am deeply grateful to my two special friends, Mrs. Annu and Mrs. Sneha, for all their co-operations at different stages. They have always given me a happy distraction to keep my brain outside of research. Their incredible friendship shall never be forgotten. I extend my honest mention of thanks to all my old friends Ms. Isha, Mr. Prashant, Mr. Mohsin and many more with whom I share a great relationship as benevolent friends. With a deep sense of reverence, I am thankful to my parents, my brother and enormously to my grandfather who have been the pillars of my life. They have always motivated me with their words of wisdom. I am also grateful to all my family members for encouraging me with their inspiring words.

Above all, I am thankful to God for giving me the ability and patience to carry on this research and completing it satisfactorily. I have been blessed with the all the nicest people, without whom this journey would not have been successful.

. . .

List of Figures

Figure	*Title*	*Page*
1.1	A schematic diagram showing amphiphilic surfactant molecules with a hydrophilic head-group and a hydrophobic tail. The surfactants are classified into four major categories based on the head-group charge.	2
1.2	A schematic diagram showing the amphiphile shape, the self-assembled structure and the respective packing parameter which is denoted by PP $(=\frac{v_0}{a_h l_c})$. This figure has been taken from [Lombardo *et al.*, 2015].	4
1.3	Structure of protein α-helix, assisted by hydrogen bond formations between the oxygen atom of the carbonyl group and the hydrogen atom of the amino group. This image has been taken from [Georgiev and Glazebrook, 2019].	6
1.4	Schematic representation of different types of $\pi-\pi$ interactions in aromatic ring systems. M+ and X- denote the cation and anion respectively.	7
1.5	Flowchart of the steps performed in the molecular dynamics simulations.	9
1.6	A schematic representation of the hierarchy of the multiscale modelling based on the length and time scale of the system. AA, UA and CG stand for all-atom, united-atom amd coarse-grained models respectively.	9
1.7	A schematic diagram showing different phases of a bilayer (a) Liquid crystalline phase (L_c), (b) Gel phase (L_β), (c) Tilted gel phase $(L_{\beta'})$, (d) Ripple phase (P_β) and fluid phase (L_α).	12
1.8	A schematic diagram showing the formation of a peptide by the linkage of amino acids and is facilitated by the elimination of water molecule.	13
2.1	Chemical structure of (a) BTMAC and (b) SA molecules in atomistic representation. Color codes: Blue, BTMAC head (N+); Ice-blue, BTMAC chains; Red, SA chains; Yellow, SA head (O); White, Hydrogen.	20
2.2	Snapshots of systems S1 to S2 (reported in table 2.2) with decreasing water concentration and the BTMAC to SA ratio at 2:1. (a)-(g) show the random initial configurations and the final configurations after self-assembly of the all systems obtained after 20 ns. Color codes: Blue, BTMAC head (N+); Ice-blue, BTMAC chains; Red, SA chains; Yellow, SA head (O); White, Hydrogen; Orange, (Cl^{-1}) and green, water. In the final configurations, all of the water molecules are not shown for the sake of clarity. Micelles are transformed into bilayers where the shape slowly changes from sphere to ellipse to bilayers. The water concentrations below which it is a bilayer is 67.28 wt %.	23
2.3	Snapshot of (a) A1 with 84.56 wt% of water and (b) A2 with 62.35 wt% water. The color code is same as used in figure 2.2 Water molecules and chloride ions are omitted for the sake of clarity.	24
2.4	Time evolution of solvent accessible surface area (SASA) for A1 and A2. The SASA is converged for the last 120 ns for both A1 and A2.	24
2.5	g(r) of head of BTMAC and SA from the center of mass of the last bead of the tails for M1, M2, M3 are shown for A1 and BA11. The distribution function from simulations with larger system-size match well.	25
2.6	Density profiles of systems A2, BA21 and BA22 which have lower water content. These systems are simulated with different box-lengths to check the system size effect.	26

2.7 Angle distribution of head-middle-end of BTMAC and SA chains for (a) systems A1 and BA11 which have higher water content (84.56 wt%), (b) systems A2, BA21 and BA22 having lower water content (62.35 wt%). The schematic representation of vectors considered to compute the angular distribution are shown in the inset of subfigure (a) where θ signifies the angle between the two vectors. 26

2.8 Time evolution of radius of gyration (R_g) of (a) M1, (b) M2, (c) M3, (d) average for system A1 after averaging over all aggregates. Error bars of R_g calculated from equation 2.4 are not shown for individual M1, M2 and M3 since their sizes are of the sizes of the symbols. Error bars of R_g calculated from R_h are shown. 28

2.9 Deuterium order parameter (S_{CD}) of (a) BTMAC (b) SA after averaging over all aggregates. S_{CD} of systems A1 and BA11 having higher water content is close to zero for both BTMAC and SA due to the spherical nature of the micelles. 29

2.10 Number of aggregations present in A1 at (a) 283 K, (b) 300 K, (c) 323 K and (d) 330 K. Different aggregates get fused together or fragmented with different temperatures. 30

2.11 Bilayer thickness (a-c) and interdigitation (d-f) superimposed on Voronoi area per head group at 283 K, 338 K and 345 K. The unit of all color bars is in nm. The plot shows the presence of rippling along y-axis till 338 K which disappears at 345 K. 31

3.1 Mapping of AA (a) BTMAC and (b) SA to CG degrees of freedom. cpk represents the AA model and the bigger spheres represent the respective CG model. VMD v1.9 [William *et al.*, 1996] is used for the snapshots. 34

3.2 Snapshot of BTMAC cylindrical micelle obtained from (a) AA simulation and (b) CG simulation of A1 using MARTINI (M), Water molecules and ions are ignored for the cause of clarity. Color codes: Purple; head, Green; tail 38

3.3 Comparison of distribution of BTMAC bonds, AA vs CG in system A1 for (a) bond-1, (b) bond-2, (c) bond-3, (d) bond-4 and (e) bond-5. 38

3.4 Comparison of distribution of BTMAC angles, AA vs CG in system A1 for (a) angle-1, (b) angle-2, (c) angle-3 and (d) angle-4. 39

3.5 g(r) of BTMAC head with respect to the centre of mass of all tails. The AA and CG g(r) match well with each other confirming the shape of the micelle to be cylindrical. 40

3.6 AA vs CG bonded distributions in system B11 for bonds in (a) BTMAC, (b) SA and for angle distributions in (c) BTMAC and (d) SA. CG BTMAC and SA bonded distributions match well with the AA ones for all models. CG angle distributions match reasonably well with the AA ones. 41

3.7 g(r) of head beads from the centre of mass of end bead for B11, showing the micellar size distributions from all CG models. Model M_b results in the best match in to the AA ones. 41

3.8 Snapshot of self-assembled spherical micelle formed from CG simulation in system B11 using M_b. Color codes: Purple; BTMAC head, Green; BTMAC tail, Red; SA head, Cyan; SA tail. 42

4.1 Area per surfactant (APS) and solvent accessible surface area (SASA) for all systems at AA and CG resolutions. The AA simulation of S8 has longer run than other systems since its per chain configurational entropy of the surfactants did not converge well until 400 ns. Similarly, the CG S8 system is simulated for 6 μs so that the SASA and APS of the system are well converged. 49

4.2 Final configurations of all asymmetric bilayers obtained from CG simulations. (a), (e), (f) and (g) correspond to bilayers S1, S5, S6 and S8 respectively obtained from biased configurations. Bilayers S2, S3, S4 and S7 obtained after self-assembly from random initial configurations are shown in (b), (c), (d) and (h) respectively. Similar configurations are observed from AA simulations. 54

4.3 AA and CG bonded distributions of BTMAC and SA in maximum asymmetry bilayer S1. (a)-(e): BTMAC bonds, (f)-(i): BTMAC angles, (k)-(n): SA bonds and (o)-(q): SA angles. AA and CG bonded distributions are in good agreement with each other. 55

4.4 Density distributions of all BTMAC and SA along the bilayer normal in system with (a, b) maximum asymmetry, (c) intermediate asymmetry (d, e) minimum asymmetry. Solid lines: AA, dashed lines: CG. red and green: two monolayers including head to tail in a chain. Black: tails excluding the head groups. Dark green : CG molecules with high entropies. 56

4.5 Bilayer thickness superimposed on the Voronoi area per head group in AA (a-c) and CG (d-f) resolutions for bilayers prepared from biased configurations. The unit of color-bar is in nm. 57

4.6 Interdigitation superimposed on the Voronoi area per head group in AA (a-c) and CG (d-f) resolutions for bilayers prepared from biased configurations. The unit of color-bar is in nm. 58

4.7 Thickness (a) and interdigitation (b) superimposed on the Voronoi cells in CG resolution for larger bilayer (S6) with intermediate asymmetry. The unit of color-bar is in nm. 58

4.8 Bilayer thickness superimposed on the Voronoi area per head group for bilayers resulting from random initial configurations with maximum and minimum asymmetries. (a), (b): AA; (c), (d): CG. The unit of color-bar is in nm. 59

4.9 Interdigitation superimposed on the Voronoi area head per group for bilayers resulting from random initial configurations with maximum and minimum asymmetries. (a), (b): AA; (c), (d): CG. The unit of color-bar is in nm. 59

4.10 Interdigitation superimposed on the Voronoi cells at AA level for bilayers with maximum asymmetry (S1), intermediate asymmetry (S5) and minimum asymmetry (S8) at 283 K (a-c), after heating to 308 K (d-f) and after cooling back to 283 K (g-i). The unit of color-bar is in nm. 61

4.11 Time evolution of per chain configurational entropy of S1 and S2 with maximum asymmetry averaged over all molecules, (a)-(d) AA, (e)-(h) CG. Molecules with higher and lower entropies are referred to as disordered and ordered molecules. The error bars represent the standard deviations in per chain configurational entropies obtained from averaging over all the molecules. 63

4.12 Time evolution of per chain configurational entropy of S5 and S6 with intermediate asymmetry, (a)-(d) AA, (e)-(h) CG. The error bars represent the standard deviation in per chain configurational entropy arising from averaging over all molecules in two classes. 63

4.13 Time evolution of per chain configurational entropy of S8 and S7 with minimum asymmetry, (a)-(d) AA, (e)-(h) CG. The error bars represent the standard deviation in per chain configurational entropy arising from averaging over all molecules in two classes. 64

4.14 Tilt vectors ($\vec{t}$) of BTMAC and SA for less and more populated leaflets for the final configurations of bilayers created using Packmol. Blue arrows: ordered molecules, green arrows: disordered molecules. (a), (b): maximum asymmetry, (c), (d): intermediate asymmetry and (e), (f) minimum asymmetry at AA resolution. Similarly tilt vector in the CG resolution is shown in (g), (h): maximum asymmetry, (i), (j): intermediate asymmetry and (k), (l). 65

4.15 Tilt vectors ($\vec{t}$) of BTMAC and SA for less and more populated leaflets for the final configurations of bilayers with random initial configuration. Bilayer S2 has maximum asymmetry whereas S7 has minimum asymmetry. Blue arrows: ordered molecules, green arrows: disordered molecules. (a), (b): maximum asymmetry, (c), (d): minimum asymmetry at AA resolution. (e), (f): maximum asymmetry; (g), (h): minimum asymmetry at CG resolution. 66

4.16 Time averaged tilt vectors ($< \vec{t} >$) of BTMAC and SA for more populated leaflets for the bilayers with (a) Maximum asymmetry, 1D ripple (system S2), (b) Intermediate asymmetry, 2D ripple (system S5) and (c) Minimum asymmetry, Gel phase (system S8). The tilt vectors are superimposed on the bilayer thicknesses. The unit of colorbar is in nm. 67

4.17 Time averaged tilt angles superimposed on the Voronoi cells of less and more populated leaflets in AA resolution for the bilayers with lamellar phase as the configuration (a), (b): maximum asymmetry; (c), (d): intermediate asymmetry and (e), (f) minimum asymmetry in AA resolution. Similarly (g), (h): maximum asymmetry; (i), (j): intermediate asymmetry and (k), (l) minimum asymmetry in CG resolution. The unit of colorbar is in degree(°). 68

4.18 Time averaged tilt angles superimposed on the Voronoi cells of less and more populated leaflets for the bilayers with random initial configurations. (a)-(d) AA, (e)-(h) CG. The unit of colorbar is in degree(°). 69

4.19 Time averaged tilt angles superimposed on the Voronoi cells of (a)-(b) AA and (c)-(d) CG bilayer S4. The unit of colorbar is in degree(°). 70

4.20 Order parameters, P_2, for two monolayers for all the systems in (a) AA and (b) CG resolution. P_2 across two layers are shown in same location to describe the difference in P_2 between the two leaflets. (c) and (d) show the differences in order parameters (ΔP_2 with respect to asymmetry percentage at AA and CG levels respectively. 71

4.21 Variation of per chain configurational entropy with asymmetry at AA resolution: (a) BTMAC, (b) SA and CG resolution: (c) BTMAC, (d) SA. The data point shown in star: S6 bilayer with larger system size. $S_{conf}^{per-chain}$ increases with increasing asymmetry percentage. The error bar represents the standard deviation around time-frames over which $S_{conf}^{per-chain}$ converged and over all molecules. 72

4.22 Variation of per chain configurational entropy with bilayer thickness (a)-(b) and interdigitation (c)-(d). Black: AA, red: CG. The data point shown in star: S6 bilayer with larger system size. $S_{conf}^{per-chain}$ increases with bilayer thickness and decreases with interdigitation. The error bar represents the standard deviation around time-frames over which $S_{conf}^{per-chain}$ converged and over all molecules. 72

4.23 Variation of per chain configurational entropy with $(1 - P_2^2)$ at AA resolution: (a) BTMAC, (b) SA and CG resolution: (c) BTMAC, (d) SA. The data point shown in star: S6 bilayer with larger system size. The error bar represents the standard deviation around time-frames over which $S_{conf}^{per-chain}$ converged and over all molecules. 73

5.1 Snapshots of P-1 (a) monomer and (b) parallel slipped stacked dimer. Color codes: Red, oxygen; Green, carbon; Blue, nitrogen and White, hydrogen. For clarity, two monomers are shown in green and yellow and P-1 nitrogens are shown in blue. 79

5.2 A schematic representation of (a) right handed helix (anticlockwise rotation) and (b) left handed helix (clockwise rotation). The orientations of the helices are similar as discussed in [Xu *et al.*, 2017]. 79

5.3 Initial snapshots of dimers with (a) positive inter-planar angle, (b) negative inter-planar angle. The inter-planar angle is the angle between the two vectors formed by joining the nitrogen atoms of the PDI cores. (c) RH and (d) LH (referred in figure 2) showing different stackings (CC/π or CH/π or T type π-interactions) with shortest distances. 80

5.4 Stacking energies of P-1 dimers upon changing the inter-planar angle without and with dispersion corrections. (RH) and (LH) dimers correspond to anticlock-wise and clockwise inter-monomer rotations respectively. 80

5.5 Snapshot of initial configurations of P-1 dimers with (a) positive inter-planar angle (RH) and (b) positive inter-planar angle (LH) solvated in water. Water molecules are shown in green color. 81

5.6 Normalized UV-vis absorption spectra obtained for 3% (7.5 μ M) THF-Water solvent. The absorption peak at 500 nm corresponds to $\pi - \pi$ stacking interactions between the P-1 monomers in the self-assembled super-structure. 83

5.7 Snapshots of dimers with (a) positive inter-planar angle (RH) and (b) negative inter-planar angle (LH) from molecular dynamics simulations. Green dots: water. Side aromatic Phe rings in the P-1 molecule are labeled from 1-8. Snapshots of dimers with (c) positive and (d) negative inter-planar angle showing hydrogen bonding in P-1 dimers. Dotted black and blue lines represent π-stacking and hydrogen bonding respectively. Water are not shown for the sake of clarity. 85

5.8 Radial distribution function, g(r), of the center of mass of PDI core and side rings (Phe motif) of dimers with (a) positive inter-planar angle, RH and (b) negative inter-planar angle, LH. Black dashed line denotes the distance for π-stacking interactions. 86

5.9 Distribution of inter-molecular angle for (a) positive inter-planar angle, RH and (b) negative inter-planar angle, LH dimers. Rings only within π-stackings are considered. The cartoon diagrams (1), (2) and (3) schematically show orientations of Phe motifs for π-stacking 87

5.10 Distribution of hydrogen bonds formed in P-1 obtained from MD simulations for LH (negative) and RH (positive) interplanar angle dimer. 87

5.11 Distributions of non-bonded energies of dimer with positive (RH) and negative (LH) inter-planar angle. (a) Coulombic energy, (b) Lennard-Jones interaction energy and (c) total non-bonded potential energy. 88

5.12 The overlapping histograms for (a) LH dimer and (b) RH dimer each obtained after 10 ns of umbrella sampling simulations in the presence of 10%THF-water and THF solvents respectively. 89

5.13 Potential of mean force (PMF) of dimer with negative (LH) and positive (RH) inter-planar angle in THF and 10% THF-water respectively. The inset shows the minima for them. 90

5.14 Snapshots of (a) negative (LH) and (b) positive (RH) dimer corresponding to the configurations with minimum potential of mean force obtained from umbrella sampling simulations in the presence of 10% THF-water and THF respectively (figure 5.13 inset). Dotted black and blue lines represent π-stacking and hydrogen bonding respectively. Solvent molecules are omitted for the sake of clarity. 91

5.15 Radial distribution function ($g(r)$) of PDI rings and side aromatic rings in (a) positive (RH) dimer in pure THF and (b) negative (LH) dimer in presence of 10% THF-water. 91

5.16 Hydrogen bond distribution in LH and RH dimers in the presence of 10% THF-water and pure THF solvents. 92

5.17 Radial distribution function of water and THF near (a) PDI rings and (b) side rings for the negative (LH) and positive (RH) dimers. 93

6.1 (a) Open and (b) Folded PyKC dimer conformers drawn using ChemDraw. These two structures are the initial configurations for the geometry optimization. 97

6.2 The initial stacked configurations of (a) open PyKC dimer and (b) folded PyKC dimer, configurations of stacked PyKC dimers obtained after geometry optimization using dispersion corrections for (c) open and (d) folded chains, (e) geometry optimized structure of folded PyKC dimer with dispersion correction. The pyrene rings stack in a parallel fashion and contribute towards $\pi - \pi$ stacking (H-type). (f) Snapshot of two stacked folded PyKC dimers obtained after the geometry optimization. For clarity, the pyrene rings are shown in magenta color. The rings participate in both H-type and T-type of $\pi - \pi$ stacking and thus have strong stacking energy. 99

6.3 Time evolution of (a) potential energy and (b) solvent accessible surface area (SASA) to examine the equilibration for the system. 100

6.4 Snapshot of PyKC folded dimers in presence of water (green color) obtained from the MD simulation. Well-defined interfaces of water and PyKC can be seen which manifest the compartmentalization of PyKC and water. The inset in figure shows the intramolecular hydrogen bonding within the peptide conjugate and the $\pi - \pi$ stacking operating across the pyrene moities which are responsible for the stability and self-assembly of PyKC in water. 101

6.5 Density profile across the normal of PyKC layers obtained from MD simulation. Interfaces of PyKC and water layers are evident which show the presence of compartments of PyKC hydrogel and water. The hydrophilic atoms (N/O) of PyKC stay buried inside the layer and drive few water molecules into the core. The water molecules which continuously stay near the inner core of PyKC layer are referred to as trapped water (TW) and shown within the area designated as (a). 102

6.6 (a) Time evolution of the intramolecular hydrogen bonds between N and O atoms of PyKC are calculated for the production run which are responsible for the stability of the molecular arrangement of the hydrogel. (b) The time evolution of the intermolecular hydrogen bonds between trapped water molecules (TW-TW), and among the amphiphilic moities of PyKC and trapped water molecules (TW-NH and TW-O). The intermolecular hydrogen bonds are computed for the time regime for which the TW molecules remain confined inside the PyKC core. 103

6.7 $g(r)$ of pyrene-pyrene determines the most probable location at $\sim$0.42 nm which corresponds to the distance of $\pi - \pi$ interactions. 103

6.8 Comparison of mean square displacements of bulk water (BW) and trapped water (BW). BW obeys diffusive behavior whereas TW shows a sub-diffusive behavior which regards to the slow dynamics of trapped water molecules. 104

6.9 Hydrogen bond auto-correlation function ($C_{HB}(t)$) of trapped and bulk water molecules. Slow relaxation of TW is evident from the time variation of $C_{HB}(t)$. Longer relation time (τ_{HB}) and high activation energy for breaking of a hydrogen bond ($\Delta G^{\#}_{break}$) for TW lead towards a slow transport of water molecules across the supra-molecular hydrogel. 105

A1 Density distributions of chloride ions and BTMAC head-groups obtained from AA simulation for equilibration and production runs. The ions reside near the BTMAC heads via electrostatic interactions and thus the location of ions do not change for both the run-lengths. 108

A2 Density distributions of chloride ions and BTMAC head-groups obtained from CG simulation for equilibration and production runs. The ions stay closer to the BTMAC heads via electrostatic interactions and thus the location of ions do not change for both the run-lengths. 108

A3 (a) Initial and (b) final snapshot of two open PyKC dimers. The open chain dimers adopt a folded conformation after simulation in an NPT ensemble. 109

List of Tables

Table	*Title*	*Page*
2.1	Masses and charges of atoms of BTMAC and SA used in the atomistic simulations. These parameters are taken from the previously studied system [Debnath *et al.*, 2009].	21
2.2	Number of molecules of BTMAC, SA and water used in different water concentrations investigated. BTMAC to SA ratio is fixed at $2:1$. The percentage of water decreases from S1 to S2.	21
2.3	Number of molecules of BTMAC, SA and water in different systems investigated. BTMAC to SA ratio is fixed at $2:1$ in A1 and A2. The percentage of water decreases from A1 to A2.	22
3.1	Number of molecules in systems A1, B1 and B11.	35
3.2	Definition of bead type in the MARTINI model	36
3.3	Mapping scheme for coarse-grained simulation	36
3.4	Non-bonded parameters used in CG B11 where M, M_a and M_b represent the MARTINI model and their modifications respectively. PM is the polarizable MARTINI water model.	39
4.1	Compositions, initial and final configurations, run-lengths and asymmetry percentage of systems investigated. The asymmetry in each system is computed using equation 4.1. The asymmetry percentage remains unchanged from AA to CG scales except S5 which has a standard deviation of 0.77% in asymmetry.	48
4.2	Area per surfactant molecule (APS) (nm^2) and volume per surfactant (VPS) (nm^3) of simulated bilayers at AA and CG resolutions. M_p and L_p denoted the more and the less populated leaflets respectively. Standard deviations of APS at AA and CG resolutions are 0.001 and 0.0002-0.0003 respectively. [a][Lunkad *et al.*, 2017], [b][N Stelter and Keyes, 2017], [c][Boek *et al.*, 2005a].	49
4.3	Extent of interdigitation ($O_{overlap}$) of simulated bilayers at AA and CG resolutions. S6 is prepared only for CG runs as the system size is large.	53
4.4	Bilayer thickness (in nm) from AA and CG simulations.[a][Lunkad *et al.*, 2017], [b][Ritwiset *et al.*, 2016], [c][Khakbaz and Klauda, 2018], [d][Zhao *et al.*, 2019], [e][Takahashi *et al.*, 1997].	60
4.5	Average single chain configurational entropy, $S_{conf}^{per-chain}$, (JK^1mol^{-1}) with standard deviations calculated from time-frames over which $S_{conf}^{per-chain}$ converges and all molecules of BTMAC and SA in AA and CG simulations. All the values are rounded off to their nearest integers and the standard deviations smaller than 0.1 are not reported here.	62
4.6	Average order parameter, $\|S_{CD}\|$ of simulated bilayers at AA resolutions. [a][Debnath *et al.*, 2009], [b][Lunkad *et al.*, 2017], [c][Khakbaz and Klauda, 2018], [d][Zhao *et al.*, 2019], [e][Davis, 1979]	70
4.7	Average order parameter, P_2 of simulated bilayers at AA and CG resolutions.	71
5.1	Binding energies (kcal mol^{-1}), angles ($^\circ$) and distances (Å) for the RH and LH dimers. The results are compared with reported values for similar PDI analogues and PDI derivatives. [Ahmed *et al.*, 2017][a], [Oltean *et al.*, 2013][b], [Chen *et al.*, 2015][c].	84
5.2	Non-bonded energies, closest distance and inter-planar angle of dimers with positive (RH) and negative (LH) inter- planar angle from molecular dynamics simulations.	88

6.1 Energies of the open and folded dimers, stacked dimers and their stacking energies obtained from the DFTB calculations. The folded PyKC conformer has a stronger stacking energy. The inter-planar distances obtained after DFTB geometry optimization and PXRD experiment [Singha *et al.*, 2019] are in good agreement indicating towards the presence of $\pi - \pi$ stacking. 100

A1 Box lengths of the simulated bilayers for AA and CG simulations. 107

List of Symbols

v_0	Critical chain volume
a_h	Optimal head-group area
l_c	Critical chain length
$\vec{E}$	Electric field
μ	Dipole moment
q	Charge
α	Polarizability
V	Potential energy
k	Force constant
σ	Distance of closest approach
ϵ	Interaction strength
ϵ_0	Permittivity of free space
F	Force
m	Mass
a	Acceleration
∇	Gradient
d	Bilayer thickness
I	Interdigitation
$g(r)$	Radial distribution function
N	Total number of particles
ρ	Mean particle density
R_g	Radius of gyration
R_h	Hydrodynamic radius
I_{min}, I_{avg}	Minimum of moment of inertia and average of moment of inertia
e	Eccentricity
β	Angle between C-D bond vector and bilayer normal
S_{CD}	Deuterium order parameter
$P(q,T)$	Bonded distribution
$U(q,T)$	Coarse-grained bonded potential energy

K_B	Boltzmann constant
λ	Asymmetry
$O_{overlap}$	Extent of interdigitation
L_a	Average chain length
$S_{conf}^{per-chain}$	Per chain configurational entropy
T	Temperature
M	3N-dimensional diagonal matrix
C	Covariance matrix
$\vec{r}_{th}$	Head to tail vector
θ_{tilt}	Tilt angle
P_2	Second rank order parameter
S_0	Residual entropy
R	Universal gas constant
T_s	Kinetic energy
E	Kohn Sham energy
$E_{ME}, E_{DE}, \Delta E_{BE}$	Monomer, dimer and binding energy
$U^b(r), U^u(r)$	Biased and unbiased potential energy
ξ	Reaction co-ordinate
$u_i(\xi)$	Biased potential
$P_i^b(\xi), P_i^u(\xi)$	Biased and unbiased distribution
$F_i(\xi)$	Unbiased free energy
U_{rot}	Potential due to rotation restraint
ω	Rotation matrix
$\hat{V}$	Unit vector parallel to the axis of rotation
$\sigma_{PMF}(\xi)$	Standard deviation in bootstrapped PMF
$r^2(t)$	Mean square displacement
t, t_0	Time and time origin
D	Diffusion co-efficient
$C_{HB}(t)$	Hydrogen bond auto correlation function
τ	Relaxation time
$G_{break}^{\ddagger}$	Free energy for hydrogen bond breaking
h	Planck's constant
$<>$	Time averaging

List of Abbreviations

AA	All-atom
APS	Area per surfactant
ATB	Automated Topology Builder
B3LYP	Becke, 3-parameter, Lee-Yang-Parr
BTMAC	Behenyl trimethylammonium chloride
CG	Coarse-grained
C_nTAB	Alkyl trimethyl ammonium bromide
COM	Centre of Mass
CPK	Corey Pauling Koltun
DFTB	Density functional tight binding
DFT	Density functional theory
DLS	Dynamic Light Scattering
DNA	Deoxyribonuleic Acid
DSC	Differential Scanning Calorimetry
EPR	Electron Paramagnetic Resonance
fs	Femtosecond
GROMACS	Groningen Machine for Chemical Simulation
LH	Left Handed
LJ	Lennard Jones
MD	Molecular Dynamics
μ s	Microsecond
nm	Nanometer
NMR	Nuclear Magnetic Resonance
NPT	Constant number of particles, pressure and temperature
ns	Nanosecond
NVT	Constant number of particles, volume and temperature
P-1	Peptide-perylenediimide molecule (Phe-Phe motif and PDI core)
PBC	Periodic Boundary Conditions
PDI	Perylenediimide

phe	Phenyl
PME	Particle Mesh Ewald
PMF	Potential of mean force
ps	Picosecond
RDF	Radial Distribution Function
RH	Right Handed
SASA	Solvent Accessible Surface Area
SA	Stearyl alcohol
SAXS	Small-angle X-ray Scattering
SCC	Self-Consistent Charges
SDS	Sodium dodecyl sulphate
SPC/E	Simple Point Charge/Extended
SPC	Simple Point Charge
THF	Tetrahydrofuran
UV-vis	Ultraviolet visible spectroscopy
VDW	van der Waals
VMD	Visual Molecular Dynamics
VOTCA	Versatile Object-Oriented Toolkit for Coarse-Graining Applications
VPS	Volume per surfactant
V-Rescale	Velocity rescale